UNIVERSITY of CALIFORNIA
SANTA CRUZ

THE ORIGIN OF LIGO SOURCES: UNDERSTANDING THE FORMATION CHANNELS OF STELLAR MASS BINARY BLACK HOLES

A thesis submitted in partial satisfaction of the
requirements for the degree of

BACHELOR OF SCIENCE

in

PHYSICS

by

Martin Lopez Jr.

10 June 2018

The thesis of Martin Lopez Jr. is approved by:

Professor Enrico Ramirez-Ruiz
Advisor

Professor Alexander Sher
Senior Theses Coordinator

Professor Robert P. Johnson
Chair, Department of Physics

Abstract

The Origin of LIGO Sources: Understanding the Formation Channels of Stellar Mass Binary Black Holes

by

Martin Lopez Jr.

LIGO detected gravitational waves (GWs) on September 14, 2015 from a binary black hole (BBH) merger. Currently, $\chi_{\rm eff}$ is the observable produced from detections used to infer the formation channel history. This is predicated on the assumption that $\chi_{\rm eff}$ is a fixed quantity from formation to merger and ultimately detection. This thesis explores the possibility that BBHs in dense stellar systems such as globular clusters (GCs) can have their $\chi_{\rm eff}$ altered through tidal disruption events (TDEs). Following disruption, a portion of mass is ripped off of the star and becomes bound to either one or both of the BHs. This mass can be accreted onto the BHs and alter the magnitude and direction of the individual BH spins, effectively changing $\chi_{\rm eff}$. We used 3D Smoothed Particle Hydrodynamics (SPH) to simulate 3 unique BBH TDE scenarios. Our simulations comprehensively cover the possible outcomes of BBH TDEs and are called the *circumbinary scenario* (CS), the *single scenario* (SS), and the *overflow scenario* (OS). Additionally we simulated a configuration called the *massive overflow scenario* (MOS) which is not unique but can provide significantly more spin up than the other scenarios. Our simulations resulted in a spin up of [(0.071, 0.071), (0,0.05), (0.051, 0.013), and (0.287, 0.407)] respectively where the given notation is $(S_{1,f}, S_{2,f})$ where $S_{i,f}$ is the final spin magnitude for the ith BH for a given scenario. The BBHs had final alignments of (aligned, NA, anti-aligned, anti-aligned) respectively. We have shown that it is possible to significantly alter the spin magnitudes and directions of LIGO BBHs (LBBHs) and thus these events must be taken into account when interpreting $\chi_{\rm eff}$ in LIGO detections.

Contents

List of Figures

To the oppressed brothers and sisters around the world and in our communities. To the black and brown lives who were always made to feel they were never good enough to succeed. To those who are fighting for justice and peace.

Acknowledgements

All praise and thanks is due to God. Nothing happens except through His will. Any success or benefit comes solely from Him and any deficiencies or mistakes are only my own. I want to thank my family for their support throughout my years at UCSC, especially my wife Samantha. She has dealt with the massive time and effort demanded of me by school over the years. I am blessed to have an amazing woman like her by my side. I would like to thank everyone a part of SLUG (Supercomputer Lab for UnderGraduates) for providing an environment of growth, friendship, and ambition. The benefit SLUG has made during my time at UCSC is immeasurable. I want to thank Enrico for always believing in me and advocating for me and pushing me to achieve excellence. Enrico is not just an outstanding mentor but he is also an outstanding human being who cares about the well-being and success of those around him. I could not have been blessed with a better advisor. Special thank you to Aldo Batta who has been my mentor alongside Enrico. Aldo has offered me countless hours of help, advice, counsel, and mentorship. He is a kind soul who is always looking to help others in need and I pray for the best for him and his family. Thank you to my collaborators for their help in this work and providing valuable insight along the way. Thank you to the numerous people I have benefited from including Phil, Jaime, Professor Prochaska, Professor Murray-Clay, and all of my community college professors. Special shout-out to Phil who guided me on how to read papers, look for new papers, understand fundamental physical concepts, and has been a great friend during my time at UCSC. Thank God.

Chapter 1 Introduction

1.1 Motivation

On September 14, 2015 the Laser Interferometer Gravitational-Wave Observatory (LIGO) detected gravitational waves (GWs) for the first time in history [1]. The source of GW150914, the detection name, was the merger of a stellar mass binary black hole (BBH), the first direct observation of a BBH merger. The monumental detection by LIGO was made possible through a century of theoretical, computational, and instrumentation developments. Since GW150914, five of the six subsequent LIGO detections have been of BBH mergers, the exception being a double neutron star (NS-NS) binary merger [2]. Therefore, the focus of this thesis will be of questions related to BBHs. A few main questions being actively researched are: (1) What processes, evolutionary or dynamic, lead to the formation of BBHs? (2) What mechanisms within these formation channels get BBHs close enough to merge through GW radiation? (3) Are there any characteristic observables upon detection that can discriminate between different possible formation channels. The main purpose of this thesis pertains to question (3).

The measured parameter which is thought to hold the key to the formation channel history of BBHs is $\chi_{\rm eff}$ [3, 4, 5]. $\chi_{\rm eff}$ is the mass weighted sum of the individual spin magnitudes projected onto the orbital angular momentum vector of the binary, as shown in Fig. 1.1 [4]. Spin is the rotation of an individual BH about its center of mass, similar to the daily rotation of the Earth.

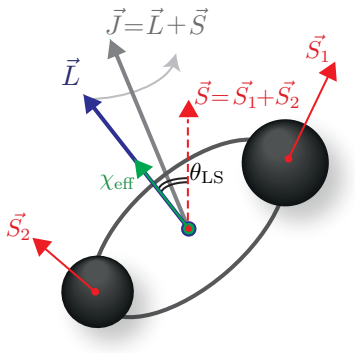

Figure 1.1: A visualization of the angular momentum vectors in a BBH system. $\vec{S}_1$ and $\vec{S}_2$ are the spin vectors of an individual BH. $\vec{L}$ is the angular momentum vector of the binary orbit. $\chi_{\rm eff}$ is the scalar quantity of the projection of the $\vec{S}$ onto $\vec{L}$.

By using 3D Smoothed Particle Hydrodynamic (SPH) simulations, we show how stellar material which is accreted following a tidal disruption event (TDE) can change $\chi_{\rm eff}$. We present the first simulations that show TDEs can significantly alter the birth spin magnitudes and orientation of the individual BHs, possibly aligning them. Through spin alignment or anti-alignment, the expected $\chi_{\rm eff}$ value from certain formation channels can be altered. Due to the fact that $\chi_{\rm eff}$ is used as a signature of formation channels, this can significantly affect the accuracy of inferring the formation history of LIGO BBHs (LBBHs). If TDEs can cause a degeneracy in $\chi_{\rm eff}$ values for different formation channels, then another way to discriminate between them must be sought. Therefore, our results will help us better understand how to interpret $\chi_{\rm eff}$ at the time of detections, crucial for gaining insight into the origin of LIGO sources.

The introduction of this thesis is outlined as follows: Section 1.2 gives a brief overview of GW history, Section 1.3 presents the currently proposed formation channels of BBHs and their expected $\chi_{\rm eff}$ values in addition to how TDEs can alter this expected value, and Section 1.4 outlines the material in the rest of the thesis.

1.2 History of Gravitational Waves

BHs constitute the most extreme physical conditions known, where the gravitational pull is so strong such that not even light can escape. The first documented proposal of such an object was by Rev. John Michell in 1784 through a Newtonian approach [6]. In 1916, Karl Schwarzschild produced the exact solutions to Einstein's field equations of general relativity for what later became known as a non-rotating BH [7]. Kerr later generalized the solutions to describe spinning BHs in 1963 [8]. Stellar mass BHs are created when all of an object's mass directly collapses to a singular point [9]. In 1916, Einstein predicted GWs by showing that they are the solutions to the field equations of gravitation [10]. GWs are transverse waves which travel at the speed of light, proven by the recent simultaneous GW and electromagnetic detections of a NS-NS merger on August 17, 2017 [11]. The properties of their GW emission and possible sources were discussed by Einstein in 1918 [12]. If the separation of a binary is small enough, gravitational radiation causes the orbit to decay eventually leading to a merger within a Hubble time, approximately the age of the universe. The first indirect evidence of GWs was achieved in 1982 after years of monitoring PSR 1913+16, a NS-NS binary system which was first discovered in 1974 [13]. PSR 1913+16 was the first observation of a binary with decaying separation consistent with GW emission [14]. The pursuit to directly detect GWs promptly commenced with the building of TAMA-300 [15], GEO600 [16], LIGO [17], and VIRGO [18].

In addition to detectors, an essential tool to observe GWs is the prediction of their waveform by solving Einstein's field equations. The formidable task of producing solutions was accomplished through analytic approximations. This is achieved by expanding in orders of v/c, where v is the speed of the object producing GWs and c is the speed of light. Such expansions are called post-Newtonian (PN) formalism. While analytical methods are able to produce solutions with contributions from orders up to 7.5PN [19], generating solutions numerically has played a pivotal role in providing waveforms. Analytic methods are not adequate for solutions during the actual merger, whereas numerical solutions are not bound by such restrictions. The first breakthrough in numerical relativity,

where the code converged to a solution, came in 2005 [20].

Technological advancements in instrumentation design and computational power precipitated the construction of Advanced LIGO (aLIGO) in 2012 [21]. Two detectors situated in Hanford, WA and Livingston, LA make up aLIGO. Having detectors in two locations helps eliminate false-positives and improves localization of sources. Improvements in sensitivity and match-filtering detector inputs through waveform templates allowed aLIGO to usher in the age of GW astronomy.

1.3 Binary Black Hole Formation Channels

There are three formation channels at the forefront of BBH theory: *common envelope evolution* (CEE), *chemically homogeneous evolution* (CHE), and the *dynamical formation channel* (DFC). CEE and CHE constitute the broad categorization of the field formation channel (FFC).

1.3.1 Field Formation Channels

Common Envelope Evolution

CEE is a complex processes that involves a series of stellar evolutionary events. In this channel stars are born within a binary in a galaxy, also known as "the field". The stars age, expand, and begin to exchange mass from outer layers of their envelopes. Mass exchange strips the most massive star of its hydrogen envelope, transforming it into a compact He star. The compact He star continues to fuse heavier elements until it directly collapses to a BH. At this stage the binary is composed of a BH and the remaining star. This star evolves and proceeds to expand until its envelope engulfs the BH, commencing the common envelope phase. The envelope slows down the BH causing it to inspiral, decreasing the separation of the orbit. The envelope is heated due to the BH piercing through it. This injection of thermal energy causes the envelope to be ejected. What is left is a tight binary composed of a compact He star and BH. The He star collapses to a BH, forming a tight BBH which can merge within a Hubble time through GW radiation [22, 23, 24, 25, 26, 27, 28, 29, 30, 31, 32].

Chemically Homogeneous Evolution

Similar to CEE, CHE begins with stars formed in a binary. The difference with CEE is that these binaries have extremely small separations such that the stars are touching. In addition to the decreased separation, the stars within these contact-binaries are rapidly rotating. The source of their rotation is either from mass accreted onto the stars or tidal torque spin up [33, 34, 35, 36, 37, 38, 39]. The rotation allows for the hydrogen that would typically be left in the outer shells of the envelope to mix throughout and burn in the core. Hydrogen mixing and burning continues until the envelope is chemically homogeneously composed of He. The burning of elements continues until both stars collapse to BHs which can merge through GW radiation. CHE is a pathway to form and merge BBHs that does not rely on the highly uncertain physical processes that plague the CEE channel [40, 36, 41, 42, 43, 32].

1.3.2 Dynamic Formation Channel

The DFC is where two/three/four body interactions in dense stellar systems, such as globular clusters (GCs), lead to BBH formation. Multiple single star-single star, single star-binary and other higher order interactions and exchanges ultimately conspire to create BBHs from existing single BHs. Further dynamical processes kick out the newly formed BBHs from the GC which allows them to merge through GW radiation without further dynamical perturbations [44, 45, 46, 47, 48, 49, 4, 50].

1.3.3 Characteristic $\chi_{\rm eff}$

Astrophysicists theorize that formation channels have a unique spin ($\chi_{\rm eff}$) signature which can be used to distinguish them at the time of merger. The spin measurements of BBHs that come from the FFC are expected to be aligned with the orbital angular momentum vector [40], resulting in a $\chi_{\rm eff} \geq 0$. The spins of BBHs from the DFC are expected to be randomly misaligned due to the isotropic nature of the multi-body interactions [4]. Therefore, the $\chi_{\rm eff}$ distribution from the DFC

are evenly scattered about zero, $-1 \leq \chi_{\rm eff} \leq 1$. It is assumed that once BBHs form through a specific channel, $\chi_{\rm eff}$ is a fixed quantity until detection. This thesis proposes that $\chi_{\rm eff}$ is actually a dynamic quantity during the life BBHs in dense stellar systems through TDEs which can change the magnitude and direction of individual birth spins.

1.4 Outline of Work

Section 2 presents the dynamics of single and binary BH TDEs and how LIGO BHs deviate from the typical treat of supermassive BH TDEs. Section 3 discusses the hydrodynamic formalism of our simulations, along with the how we set up our initial conditions for each simulation. Additionally, this section details the results of each simulation, the final spin magnitudes, and $\chi_{\rm eff}$. Section 4 discusses the implications of our results and summarizes our work.

Chapter 2 Tidal Disruption Events by LIGO BHs[1]

2.1 Tidal Disruption Events

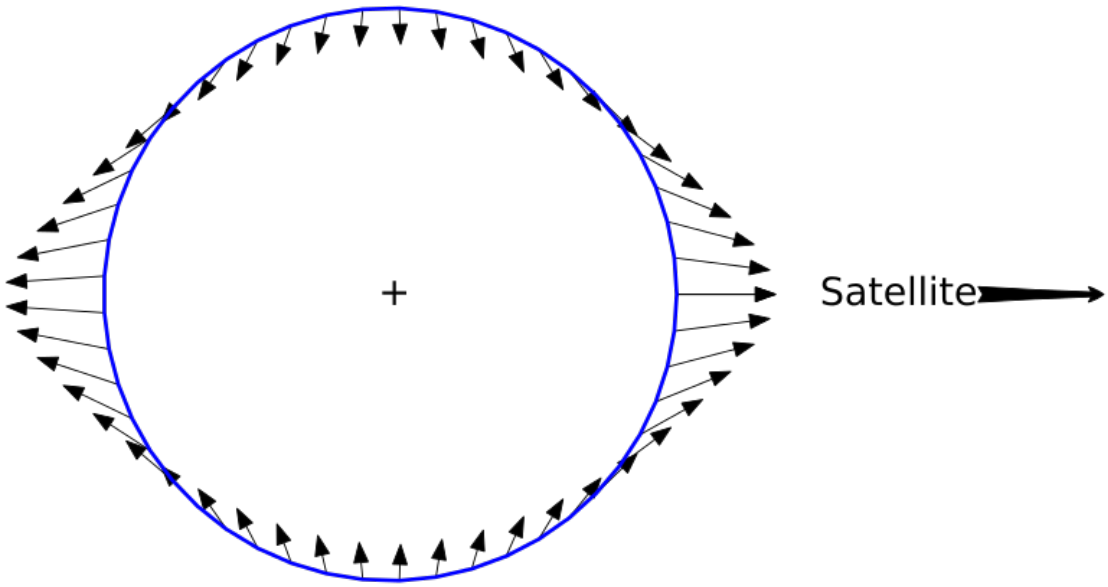

Figure 2.1: This figure shows the effect of the tidal field on a body due to a satellite object. The force of gravity on the body closest to the satellite is stronger than the force of gravity on the opposite side of the body causing tidal distortions on the body.

A body, specifically a star, which feels the force of gravity from a massive object, specifically a BH, is subject to distortions due to the tidal field of the BH as shown in Fig. 2.1 [51]. The tidal

[1]The majority of this chapter comes from Lopez Jr. et al (to be submitted to ApJL 2018)

force, F_τ, is the gradient on the gravitational force across the star defined as

$$F_\tau = \frac{G\mathrm{M_{bh}M_\star}}{r^3}\mathrm{R_\star} \tag{2.1}$$

Where G is the gravitational constant, $\mathrm{M_{bh}}$ is the mass of the BH, $\mathrm{M_\star}$ and $\mathrm{R_\star}$ are the mass and radius of the star, respectively. In order to get the tidal radius, R_τ, at which the tidal force is equal to the force of gravity holding the star together, we set the forces equal and solve for the distance as

$$\begin{aligned} F_g &= F_\tau \\ \frac{G\mathrm{M_\star^2}}{\mathrm{R_\star^2}} &= \frac{G\mathrm{M_{bh}M_\star}}{\mathrm{R_\tau^3}}\mathrm{R_\star} \\ \mathrm{R_\tau^3} &= \frac{\mathrm{M_{bh}}}{\mathrm{M_\star}}\mathrm{R_\star^3} \\ \mathrm{R_\tau} &= \left(\frac{\mathrm{M_{bh}}}{\mathrm{M_\star}}\right)^{1/3}\mathrm{R_\star} \end{aligned} \tag{2.2}$$

Supermassive BHs (SMBHs) ($\mathrm{M_{bh}} \gtrsim 10^6\mathrm{M_\odot}$, where $\mathrm{M_\odot}$ is the mass of the sun) at the center of galaxies where stars in the galactic nuclei are dominated by the potential of the SMBH in addition to the potential of all the surrounding stars lead to frequent parabolic orbits around the SMBH with pericenter distances equal to the tidal radius [52, 53, 54]. For globular clusters where stellar mass BHs are the dominant type, mass segregation in which the heaviest members (ie. BHs) of the cluster sink to the center [55] increase the number density by orders of magnitude making the tidal disruption events rate higher than those in galactic nuclei [56].

2.1.1 Single BH Dynamics

Canonical TDEs occur when a star with mass M_* and radius R_* gets disrupted when approaching a SMBH with mass $M_{\rm bh}$ at a pericenter distance $R_{\rm p} = R_\tau = q^{-1/3}R_*$, where $q = M_*/M_{\rm bh}$. After the disruption, about half of the star becomes unbound and ejected, while the other half becomes bound to the SMBH on elliptical orbits. 3D hydrodynamical simulations have

quantified the rate at which material falls back onto the SMBH. A good fit to observed light curves of TDEs is obtained if one assumes that the accretion luminosity directly follows the fallback rate in the simulation [57]. However, it is not clear why this should be the case. Bound debris returns to the SMBH with a large range of eccentricities and orbital periods [58] and it may take many Keplerian orbits for fallback material to circularize and accrete [59]. Some mechanism is therefore required to quickly dissipate the kinetic energy of the fallback material and circularize it into an accretion disk.

In standard TDE discourse, the disrupting SMBHs have masses $M_{\rm bh} \gtrsim 10^6 M_\odot$ yielding $q \ll 1$, which allows the semi-major axis of the most bound material to be approximated as:

$$\begin{aligned} a_{\rm mb} &= \left(\frac{\mathrm{M_{bh}}}{\mathrm{M_\star}}\right)^{1/3} \mathrm{R}_\tau \\ &= q^{-1/3}\ \mathrm{R}_\tau. \end{aligned} \tag{2.3}$$

However for LBBHs, the mass ratios are near unity, making the extent of the star comparable to the tidal radius. In order to properly derive the semi-major axis of material a radius r from the center of the star we need to first get the energy of that material, $E(r)$. The star is on a parabolic orbit such that the center of mass (CM) energy at pericenter is zero. For the reference frame where the BH is at the origin, the CM energy is defined as

$$\begin{aligned} E(\mathrm{R}_\tau) &= U_{\rm CM} + T_{\rm CM} \\ &= -\frac{G\mathrm{M_{bh}}}{\mathrm{R}_\tau} + T_{\rm CM} \\ &= -\frac{G\mathrm{M_{bh}}}{\mathrm{R}_\star} q^{1/3} + T_{\rm CM} \end{aligned} \tag{2.4}$$

where $T_{\rm CM}$ is the kinetic energy of the CM. While the energy of material a distance r from the

center, $E(R_\tau - r)$, in the same reference frame is

$$\begin{aligned} E(R_\tau - r) &= U(R_\tau - r) + T(R_\tau - r) \\ &= -\frac{G\mathrm{M_{bh}}}{\mathrm{R}_\tau - \mathrm{r}} + T(R_\tau - r) \\ &= -\frac{G\mathrm{M_{bh}}}{\mathrm{R}_\tau \left(1 - \frac{\mathrm{r}}{\mathrm{R}_\tau}\right)} + T(R_\tau - r) \\ &= -\frac{G\mathrm{M_{bh}}}{\mathrm{R}_\tau}\left(1 + \sum_{n=1}^{\infty}\left(\frac{r}{\mathrm{R}_\tau}\right)^n\right) + T(R_\tau - r) \\ &= -\frac{G\mathrm{M_{bh}}}{\mathrm{R}_\star} q^{1/3}\left(1 + \sum_{n=1}^{\infty}\left(\frac{r}{\mathrm{R}_\star}\right)^n q^{n/3}\right) + T(R_\tau - r) \end{aligned} \tag{2.5}$$

where $T(R_\tau - r)$ is the kinetic energy of stellar material at radius r. There are two key steps to deriving $E(r)$: First, we assume that the CM is moving at the same velocity as the material at $R_\tau - r$ such that the kinetic energy at these two points in the star are equal to some value T. Second, the fact that the CM energy is zero allows us to subtract $E(R_\tau)$ from $E(R_\tau - r)$ to get $E(r)$.

$$\begin{aligned} E(r) &= E(\mathrm{R}_\tau - \mathrm{r}) - \mathrm{E}(\mathrm{R}_\tau) \\ &= -\frac{G\mathrm{M_{bh}}}{\mathrm{R}_\star} q^{1/3}\left(1 + \sum_{n=1}^{\infty}\left(\frac{r}{\mathrm{R}_\star}\right)^n q^{n/3}\right) + T - \left[-\frac{G\mathrm{M_{bh}}}{\mathrm{R}_\star} q^{1/3} + T\right] \\ &= -G\mathrm{M_{bh}}\left[\sum_{n=1}^{\infty}\left(\frac{q^{1/3}}{\mathrm{R}_\star}\right)^{n+1} r^n\right], \end{aligned} \tag{2.6}$$

where r is the distance from the star's CM.

For material that is bound to the BH, this expression translates into a range of semi-major axes given by:

$$\begin{aligned} a(r) &= -\frac{G\mathrm{M_{bh}}}{2E(r)} \\ &= \left[2\sum_{n=1}^{\infty}\left(\frac{q^{1/3}}{\mathrm{R}_\star}\right)^{n+1} r^n\right]^{-1}, \end{aligned} \tag{2.7}$$

which for canonical TDEs ($q \ll 1$) can be safely approximated to first order. As q approaches unity this approximation is no longer valid and the semi-major axis of the most bound material approaches the tidal radius and becomes equal to it at a critical mass ratio $q_{\mathrm{crit}} = 0.037$. The assumption that the circularization radius of the most bound material is about twice the tidal

radius R_τ [60, 61, 62, 63, 64, 65] also breaks down in the LBBH regime. The circularization radius of the most bound material $R_{\mathrm{c,mb}}$ is obtained by equating its angular momentum, L_{mb}, to the angular momentum of a circular orbit, L_{c}, and solving for the required radius to conserve angular momentum

$$\begin{aligned} L_{\mathrm{mb}} &= L_{\mathrm{c}} \\ \mathrm{M}_\star v_{\mathrm{peri}} \left(\mathrm{R}_\tau - \mathrm{R}_\star\right) &= \mathrm{M}_\star \mathrm{R}_{\mathrm{c}} v_{\mathrm{c}} \\ v_{\mathrm{peri}} \left(R_\tau - \mathrm{R}_\star\right) &= R_{\mathrm{c}} v_{\mathrm{c}} \\ R_{\mathrm{c}} &= \left(R_\tau - \mathrm{R}_\star\right) \left(\frac{v_{\mathrm{peri}}}{v_{\mathrm{c}}}\right) \end{aligned} \tag{2.8}$$

where v_{peri} is the velocity at pericenter for a parabolic orbit, which we assumed to be equal to the velocity of the most bound material , defined as

$$v_{\mathrm{mb}} = \left(\frac{2G\mathrm{M}_{\mathrm{bh}}}{\mathrm{R}_\tau}\right)^{1/2} \tag{2.9}$$

and v_{c} is the Keplarian velocity defined as

$$v_{\mathrm{c}} = \left(\frac{GM_{\mathrm{bh}}}{R_{\mathrm{c}}}\right)^{1/2} \tag{2.10}$$

Plugging these values into Eq. 2.8 we get

$$\begin{aligned} R_{\mathrm{c}} &= \left(\mathrm{R}_\tau - \mathrm{R}_\star\right) \left(\frac{v_{\mathrm{peri}}}{v_{\mathrm{c}}}\right) \\ &= \left(\mathrm{R}_\tau - \mathrm{R}_\star\right) \left(\frac{2G\mathrm{M}_{\mathrm{bh}}}{\mathrm{R}_\tau}\right)^{1/2} \left(\frac{G\mathrm{M}_{\mathrm{bh}}}{R_{\mathrm{c}}}\right)^{-1/2} \\ &= \left(\mathrm{R}_\tau - \mathrm{R}_*\right) \left(\frac{2R_{\mathrm{c}}}{\mathrm{R}_\tau}\right)^{1/2} \\ &= \left(\frac{2}{\mathrm{R}_\tau}\right) \left(\mathrm{R}_\tau - \mathrm{R}_\star\right)^2 \\ &= \left(\frac{2}{\mathrm{R}_\tau}\right) \mathrm{R}_\tau^2 \left(1 - \frac{\mathrm{R}_\star}{\mathrm{R}_\tau}\right)^2 \\ &= 2\mathrm{R}_\tau \left(1 - \frac{\mathrm{R}_\star}{\mathrm{q}^{-1/3}\mathrm{R}_\star}\right)^2 \\ &= 2\mathrm{R}_\tau \left[1 - \mathrm{q}^{1/3}\right]^2 \end{aligned} \tag{2.11}$$

The circularization radius of the pericenter $R_{\rm c,p}$ can be similarly derived to get $R_{\rm c,p} = 2{\rm R}_\tau$ while the spread in circularization radii can be written as

$$\frac{\Delta R_{\rm c}}{R_{\rm c,p}} = q^{1/3}\left[2 - q^{1/3}\right], \tag{2.12}$$

In order for this material to circularize and form a disk, energy must be dissipated efficiently after disruption. Material falling to pericenter can be heated by hydrodynamical shocks with a fractional energy dissipation per orbit, $\nu_{\rm H}$ [65], which can be written as

$$\nu_{\rm H} = \beta q^{2/3} \tag{2.13}$$

where $\beta = R_{\rm p}/{\rm R}_\tau$. For disruptions in the LBBH regime, the energy dissipation via shocks can be sizable and lead to efficient circularization. This is contrast to the standard case with $q \ll 1$, for which hydrodynamical shocks at pericenter are likely to be insufficient and rapid circularization might only be achieved via general relativistic effects [66, 59, 67, 68].

2.1.2 Binary BH Dynamics

For BBH TDEs, the star does not necessarily follow a parabolic orbit and the orbital deviations before disruption depend strongly on the separation d and eccentricity e of the binary. The CM energy distributions of a sun-like star disrupted by a $15{\rm M}_\odot$ equal mass BBH with $e = 0.5$ are shown in Fig. 2.2 for three distinct binary separations using the N-body code developed by [69]. The properties of the binary have been selected to reflect those derived by [70] for dynamically assembled LBBHs. In this case ${\rm R}_\tau = 2.47{\rm R}_\star = 0.011{\rm AU}$. For ${\rm R}_\tau/{\rm d} \ll 1$ the CM energy is essentially parabolic while a larger fraction of unbound CM orbits are observed for tighter binaries. This is because as the star approaches the BBH, its trajectory is influenced by the combined potential of the binary and, as a result, when the star reaches ${\rm R}_\tau$ is moving faster than it would have if its orbit was parabolic.

After disruption, the fate of the debris also depends sensitively on the ratio ${\rm R}_\tau/d$. If ${\rm R}_\tau/d > 1$, the disruption will take place outside of the binary and the infalling material will form a

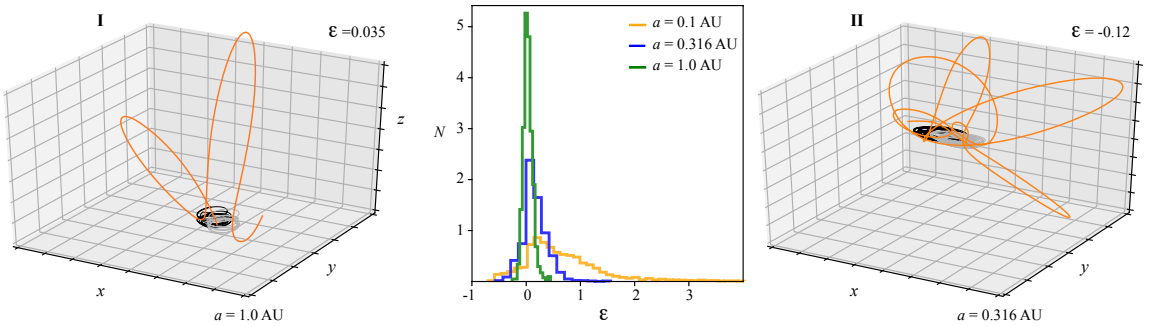

Figure 2.2: The CM energy distributions and specific trajectories are shown for a sun-like star ($M_\star = 1M_\odot$, $R_\star = R_\odot$) interacting with a $15M_\odot$ equal mass BH binary with $e = 0.5$. Here we study the outcomes of TDE interactions and their associated CM energy distributions by performing large set of numerical scattering experiments. The panels shows the energy distribution for different binary separations ($d = 1.0\text{AU} = 87.3R_\tau$, $d = 0.316\text{AU} = 27.6R_\tau$, $d = 0.1\text{AU} = 8.73R_\tau$) and the trajectories of bound (II) and unbound (I) stellar orbits (*orange* trajectories) . Here ε is the CM energy of the star at R_τ in units of the binding energy of the star.

circumbinary disk around the system. In what follows, we refer to this scenario as the *circumbinary scenario* (CS). When $R_\tau/d \lesssim 1$, the star will be disrupted by one of the binary members but the accretion history of the debris onto the system is determined by d. This is due to the disrupted debris orbiting around the disrupting BH with a wide range of semi-major axes such that there is always some material that is able to reach the sphere of influence of the companion BH. In order to determine whether or not the non-disrupting BH can accrete significant amounts of stellar debris we make use of two important characteristic scales. One is the semi-major axis a_{90} of the disrupted material whose orbit contains 90% of the stellar debris and the other one is the Roche lobe radius R_L, which determines the gravitational sphere of influence of the disrupting BH. R_L can be written [71] as

$$\frac{R_\text{L}}{d} = \frac{0.49{q_\text{b}}^{2/3}}{0.6q_\text{b}^{2/3} + \ln\left(1 + q_\text{b}^{1/3}\right)}, \tag{2.14}$$

where q_b is the mass ratio of the BBH. When $a_{90}/R_\text{L} < 1$, a small fraction of the debris is able to interact with the non-disrupting BH but most of the stellar debris will be accreted by the disrupting BH. In this case, the tidal interaction will resemble that caused by a single BH and we refer to this as the *single scenario* (SS). On the other hand, disrupted material with $a_{90}/R_\text{L} \gtrsim 1$ will be influenced by the companion and a sizable fraction of debris can be accreted by the non-disrupting BH. A case

we refer to as the *overflow scenario* (OS).

In order to calculate the spin change due to accretion of disrupted material we use [72]

$$S(M_{\rm bh,f}) = \left(\frac{2}{3}\right)^{1/2} \frac{M_{\rm bh}}{M_{\rm bh,f}} \left\{ 4 - \left[18 \left(\frac{M_{\rm bh}}{M_{\rm bh,f}} \right)^2 - 2 \right]^{1/2} \right\}, \tag{2.15}$$

which assumes an initially low or non-spinning BH. Here $M_{\rm bh,f} = M_{\rm bh} + fM_*$ is the final mass of the BH after accreting a fraction f of the disrupted star. For a TDE of a star in a parabolic orbit ($f = 0.5$), the maximum mass that the BH can accrete is $0.5\mathrm{M}_\star$ such that the maximum spin up, $S_{\rm max}$ is given by

$$S_{\rm max}(q) = \left(\frac{8}{3}\right)^{1/2} \left(\frac{1}{2+q}\right) \left\{ 4 - \left[72 \left(\frac{1}{2+q} \right)^2 - 2 \right]^{1/2} \right\} \tag{2.16}$$

The values of $S_{\rm max}$ for a few characteristic q's are $S_{\rm max}\left(q = 1 \times 10^{-6}\right) = 1.84{\times}10^{-6}$, $S_{\rm max}\left(q = 0.01\right) = 0.02$, and $S_{\rm max}\left(q = 0.5\right) = 0.60$. This clearly illustrates that for LBBHs, the digestion of stars during the lifetime of the binary could lead to noticeable spin changes.

Chapter 3 Hydrodynamics[1]

3.1 Set-Up

Our hydrodynamical simulations of BBH TDEs use a modified version of the SPH code Stellar GADGET-3 [73, 74]. GADGET-3 allows us to follow accretion into sink particles and employs a polytropic equation of state, $P = \rho^{\Gamma}$, with a structural gamma $\Gamma = [4/3, 5/3]$ for solar-like stars and giants respectively and an adiabatic gamma $\gamma = \mathrm{C_p}/\mathrm{C_v} = 5/3$, where $\mathrm{C_p}$ and $\mathrm{C_v}$ are the heat capacity at constant pressure and volume respectively. γ determines how how the star responds to perturbations instantaneously while Γ determines the global structure of the star. By solving the Lane-Emden equation, and using the same method as in [75], we created 3D spherically symmetric distributions of SPH particles mapping polytropic stars in hydrodynamical equilibrium. We ran test cases of the tidal disruption of a 1 $\mathrm{M}_{\odot}$ star by a 15 $M_{\odot}$ equal mass BBH with resolutions between 10^5 and 10^6 particles, which showed convergence for the accretion rates in the SS, OS, and MOS simulations while the amount of bound mass converged for the CS simulation.

3.2 Initial Conditions

All initial conditions (ICs) assume typical parameters for BBHs and stars in globular clusters (GCs) with $e = 0.5$, BBH parameters were taken from [70]. We further assumed that the individual spins of the BHs (S_1 and S_2) to be initially zero, which is consistent with the small spins

[1] The majority of this chapter comes from Lopez Jr. et al (to be submitted to ApJL 2018)

observed in LIGO events. By means of a 3 body code, we obtained the dynamical properties of the BBH and star prior to a tidal disruption, tracing the trajectories of all three bodies back to the time when the star lies six tidal radii away from the disrupting BH. These dynamical properties were included in the GADGET-3 initial conditions file.

3.3 Simulation Results

In Section 2.1.2 we defined three unique scenarios for BBH TDEs, the SS, CS, and OS. The SS simulation, where $d \gg \mathrm{R}_\tau$, results in an approximately single BH TDE in which only one BH accretes and the non-disrupting BH is undisturbed, results for the SS are discussed in detail in Section 3.3.1. The CS simulation where $d \ll \mathrm{R}_\tau$ creates a system of a BBH embedded in a circumbinary disk discussed further in Section 3.3.2. The final unique scenario is the OS simulation where $d \lesssim \mathrm{R}_\tau$ produces multiple TDEs where both BHs are able to accrete and is outlined further in Section 3.3.3. We have simulated one more scenario which is not unique but can provide a significant increase in spin magnitude called the 3.3.4, the differences between the OS and MOS and its results are discussed in Section 3.3.4. The parameters of each scenario are listed in Fig. 3.1 and Fig. 3.2.

3.3.1 The Single Scenario

The Single Scenario (SS) simulation is characterized by the ratios $\mathrm{R}_\tau/d = 0.01$ and $a_{90}/R_\mathrm{L} = 0.27$, which determine the negligible interaction of disrupted material with the second BH and the resemblance to a TDE with a single BH. The SS simulation is consistent with the scenario shown in Fig. 2.2 for an unbound stellar orbit. The top row panel of Fig. 3.1 shows the column density of the SS at three different times. After a fall back time scale, bound material forms an accretion disk which follows an $\dot{\mathrm{M}}$ curve similar to those of canonical TDEs simulated by [76]. However, given the mass ratio $q \lesssim 1$, the fallback time scale (given by the circularization radius) of the most bound material will differ from those shown in [76].

By the end of the simulation, the disrupting BH accreted a total mass of 0.1 $\mathrm{M}_\odot$ and has

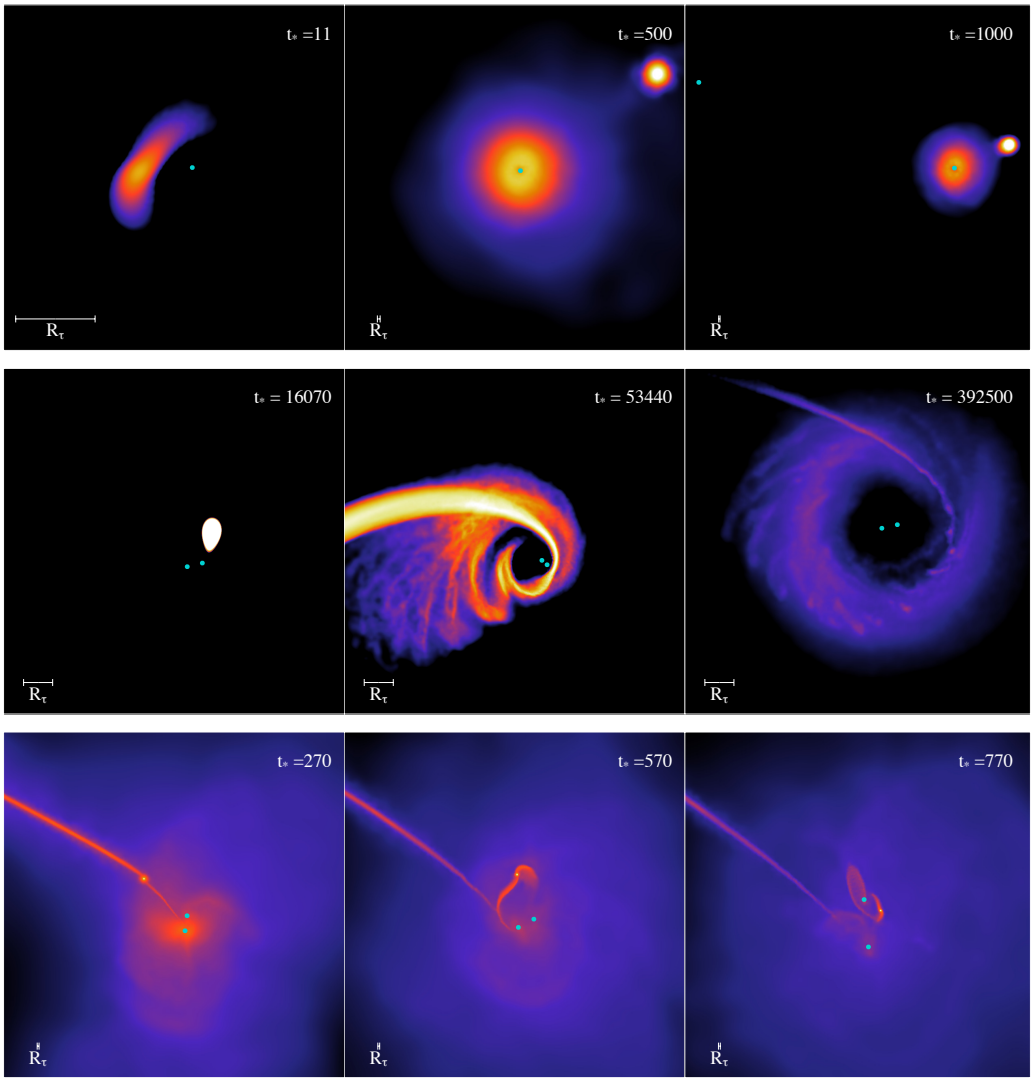

Figure 3.1: The characteristics of each unique BBH TDE scenario. t_* and R_τ are the dynamical time step and individual BH tidal radius for each panel respectively. All panels are in the orbital plane of the BBH. **Top panel (Single Scenario [SS]):** The left image is zoomed in to show the initial disruption onto one of the BHs. The middle image zooms out to show the subsequent accretion onto the disrupting BH. The right image zooms out more to show the entire BBH and the isolation of the non-disrupting BH. **Middle panel (Circumbinary Scenario [CS])** The left image shows the initial disruption occurring outside the BBH. The middle image shows the shock and stream which forms from the initial TDE. The right image shows the circularization of the disk. **Bottom panel (Overflow Scenario [OS]):** The left image is the initial disruption of the star. The middle image is the following disruption of the remaining stellar core. The right image is the third of the total four disruptions that occur in this scenario. **The parameters** of each scenario, listed as [SS,CS,OS], are: $N_{\rm particles} \approx [10^5, 10^6, 10^5]$, $\mathrm{M}_\star = [1,1,1]\mathrm{M}_\odot$, $\mathrm{R}_\star = [1,43,1]\mathrm{R}_\odot$, $\Gamma = [4/3, 5/3, 4/3]$, $\mathrm{M}_{\mathrm{BH}_1} = \mathrm{M}_{\mathrm{BH}_2} = [15,15,15]\mathrm{M}_\odot$, $d = [429.88, 42.99, 42.99]\mathrm{R}_\odot$, $v_\infty = [30,10,20]$km/s, $i = [\pi/3, \pi/4, \pi/3]$

an accretion disk whose angular momentum $J_{\rm disk}$ is at an angle 1.8 rad with respect to the orbital angular momentum of the binary $J_{\rm bin}$. Assuming that the $\sim$ 0.13 $M_\odot$ of the accretion disk are accreted by the BH, its spin magnitude could increase to $S_1 \approx 0.05$, with an orientation angle of 1.8 rad with respect to $J_{\rm bin}$, resulting in an anti-aligned effective spin of $\chi_{\rm eff} \approx -0.005$.

3.3.2 The Circumbinary Scenario

The Circumbinary Scenario (CS) simulation is shown in the middle row of Fig. 3.1. With a ratio of $R_\tau/d = 2.47$, the tidal radii of each BH overlap and encompass the BBH, resulting in a disruption where bound material forms an accretion disk around the binary. The disk rapidly circularizes and is slowly accreted onto both BHs through viscous dissipation. By the end of the simulation, the mass accreted onto each BH is 0.01 $M_\odot$ and the accretion disk has $0.59M_\odot$ whose $J_{\rm disk}$ is oriented at $(11/90)\pi$ with $J_{\rm orb}$, which we assume to be evenly accreted by both BHs. In the most optimistic scenario, this will result in a maximum $\approx 0.3M_\odot$ accreted by each of the BHs through an accretion disk, leading to spin magnitudes of $S_1 = S_2 \approx 0.071$, and $\chi_{\rm eff} \approx 0.06$.

3.3.3 The Overflow Scenario

The Overflow Scenario (OS) is shown in the bottom row of Fig. 3.1. The ratios $R_\tau/d = 0.06$ and $a_{90}/R_{\rm L} = 2.74$ imply a disruption by a single BH, and that a significant amount of bound disrupted material will reach the non-disrupting BH respectively. The OS scenario allows for accretion onto both BHs and the possibility of obtaining aligned or anti-aligned BH spins. The initial disruption of the star occurs at $\beta \approx 1.62$, leaving the core intact [76] and leading to multiple resonant TDEs.

By the end of the simulation, the mass accreted by the disrupting and non-disrupting BHs is 0.19 $M_\odot$ and 0.02 $M_\odot$ respectively. However, there's still $\sim$ 0.06 $M_\odot$ of bound to the system, which can lead to a maximum spin up of $S_1 \approx 0.051$ at an angle 0.241 rad from $J_{\rm bin}$ and $S_2 \approx 0.013$ at an angle 1.58 rad from $J_{\rm bin}$ for the disrupting and non-disrupting BHs respectively. This will lead

to a final effective parameter $\chi_{\rm eff} \approx 0.005$.

3.3.4 The Massive Overflow Scenario

The tiny change in spin magnitudes obtained from the previous scenarios is expected for solar mass stars since $S_{\rm max}\,(q = 0.067) = 0.11$. Therefore, in order to obtain a more substantial change in spin we increased q to 0.5, in what we call the Massive Overflow Scenario (MOS). The characteristic ratios for the MOS are $\mathrm{R}_\tau/\mathrm{d} = 0.35$ and $a_{90}/R_{\rm L} = 4.65$ which predict that there should be significant accretion onto both BHs. The similarities between the OS and MOS can be seen in Fig. 3.2.

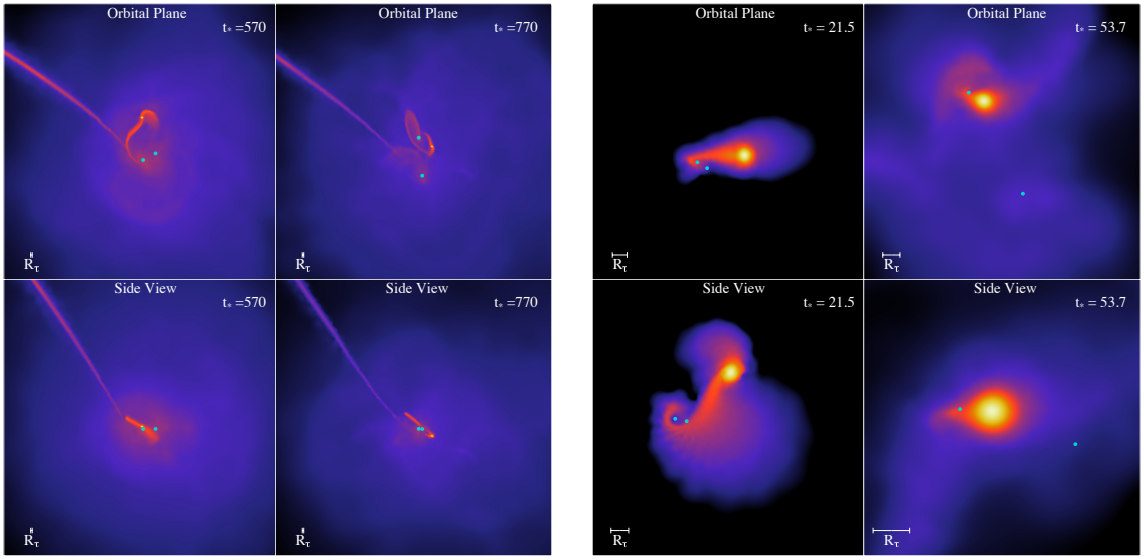

Figure 3.2: Similarities between OS and MOS. t_* and R_τ are the dynamical time step and individual BH tidal radius for each panel respectively. **Left Panel (Overflow Scenario [OS]):** The top row of the left panel are the same as those in the bottom panel of Fig. 3.1, an orbital plane view of the OS. The bottom row shows the corresponding side view of the same snapshots. The side view shows that the angle of the disk remains constant through multiple disruptions. **Right Panel (Massive Overflow Scenario [MOS]):** The top row shows the orbital view of the total two TDEs that come from the MOS. The bottom row shows the side view of the MOS and you can see a significant torque on the binary due to the high mass ratio between the star and the BBH. **The parameters** for the MOS are: $N_{\rm particles} \approx 10^5$, $\mathrm{M}_\star = 5\ \mathrm{M}_\odot$, $\mathrm{R}_\star = 6\ \mathrm{R}_\odot$, $\Gamma = 4/3$, $\mathrm{M}_{\mathrm{BH}_1} = \mathrm{M}_{\mathrm{BH}_2} = 10\ \mathrm{M}_\odot$, $d = 21.49\ \mathrm{R}_\odot$, $v_\infty = 30$ km/s, $i = \pi/3$

Both OS and MOS simulations lead to multiple disruptions and result in accretion onto both BHs as expected. However, the $\dot{\mathrm{M}}$ curves shown in Fig. 3.3 are significantly different. In the

OS panel accretion onto the disrupting BH looks pretty much like in canonical TDEs, showing a peak and a power law decay. Meanwhile, accretion onto the non-disrupting BH takes a long time to begin and is negligible. Despite the multiple disruptions observed in the bottom panels from Figure 3.1, most of the mass accreted by the BHs comes from the first disruption, and thus most of their spin. In the MOS panel, accretion onto both BHs occurs almost at the same time and both BHs have a very similar $\dot{M}$ throughout the entire simulation. In this scenario the first disruption did not lead to the maximum amount of accreted material. It is until the second disruption, when most of the material gets captured in an accretion disk around one of the BHs (labeled as BH_2 in Fig. 3.3). This accretion disk is shown in the right bottom panel of Figure 3.3, and as can be seen, the non disrupting BH is really close to this accretion disk, making it easy for it to accrete a substantial amount of material, specially since the binary orbit is highly eccentric and it will eventually plunge into the accretion disk.

The mass accreted by the BHs by the end of the simulation is 0.91 $M_\odot$ and 0.40 $M_\odot$ respectively. Once again we will assume that the ~ 1.06 $M_\odot$ bound to the system will be accreted through an accretion disk, leading to a maximum spin $S_1 \approx 0.287$ at angle 0.14 rad with $J_{\rm bin}$ for the first BH, and $S_2 \approx 0.407$ at angle 2.2 rad with $J_{\rm bin}$ for the second one, leading to a final effective parameter $\chi_{\rm eff} \approx 0.016$.

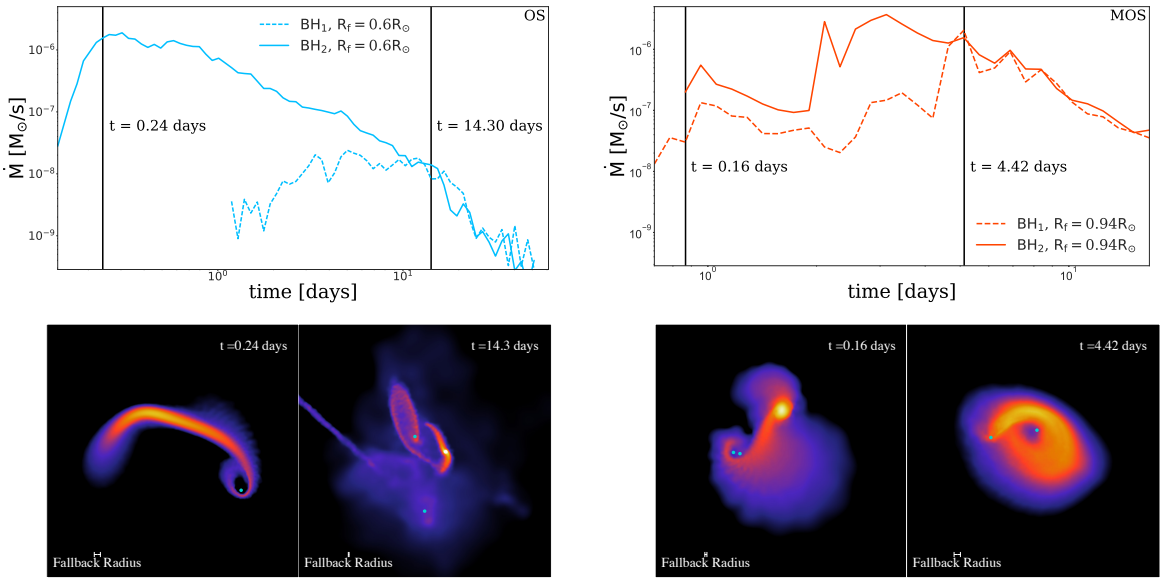

Figure 3.3: Mass accretion, $\dot{M}$, curves of the OS and MOS. The fallback radius, R_f in the plots, is the radius at which $\dot{M}$ is calculated. t is the time of the snapshot measured from initial accretion. **Left Panel (Overflow Scenario [OS]):** The plot shows the rate of mass accretion onto both BHs. The initial disruption is where the majority of stellar material is accreted. [Add part about when the secondary actually starts accreting.] While the secondary BH is accreting, the amount is negligible to the primary amount. The bottom figures show snapshots of the simulation corresponding to the vertical lines in the plot. **Right Panel (Massive Overflow Scenario [MOS]):**The plot shows the rate of mass accretion onto both BHs. This curve is in contrast to the OS because both BHs accrete significantly due to the larger amount of stellar material available. After the second disruption their curves are almost identical. This is ideal for altering the spin because we want both BHs to accrete a notable percentage of their own mass. The bottom figures show snapshots of the simulation corresponding to the vertical lines in the plot.

Chapter 4 Discussion and Summary

4.1 Spin Alignment

When accretion of material onto both BHs by a BBH TDE occurs, the spin up direction of each BH can result in relative alignment or anti-alignment. The non-disrupting BH always spins up aligned with the orbital angular momentum due to the density gradient it encounters upon accretion. Therefore, the disrupting BH will determine the relative spin alignment. The two key factors that dictate whether the disrupting BH gains spin in or opposite the direction of the orbital angular momentum are the relative motion of the disrupting BH to the star upon disruption and whether the star is disrupted outside or inside the BBH.

There are two scenarios that result in spin alignment: 1) The star is disrupted outside the BBH in the direction of the orbital velocity and 2) the star is disrupted inside the BBH in the direction against the orbital velocity. The two scenarios that result in anti-alignment are: 1) The star is disrupted outside the BBH in the direction against the orbital velocity and 2) the star is disrupted inside the BBH in the direction of the orbital velocity.

In order to calculate the probability of alignment, one of our collaborators Irvin Fabian Martinez-Rodriguez ran 35,000 N-body simulations of BBH TDEs and captured the relative angle of stellar velocity and orbital velocity along with whether the TDE occurred inside or outside of the BBH. The probability of anti-alignment is $\approx 53\%$. Along with following the mass accretion, we also tracked the angular momentum deposition onto each BH due to mass accretion. We found that

the OS and MOS simulations resulted in anti-aligned spins whereas the CS simulations results in aligned spins.

4.2 Summary

The detection of GW150914 and subsequent BBH merger detections have opened up many questions about BBH formation history. Individual BH spins and $\chi_{\rm eff}$ are often used to characterize the formation channel of BBHs. In this thesis we have explored the possibility and consequences of BBHs in dense stellar systems experiencing TDEs during their lifetime. We have shown that the accretion which follows from a TDE can spin up each BH and align or anti-align the relative spins. Additionally, LBBHs probe a new interesting regime of TDEs that significantly deviates from the canonical SMBH treatment. The typical approximations break down when trying to understand the nature of the dynamics of LBBH TDEs with respect to dissipative and orbital time scales. The chaotic behavior of these interactions require a hydrodynamical treatment to properly model LBBH TDEs. Our work has shown that the notion of dynamic spin alignments must be considered when inferring the formation channel history of LIGO sources, contrasting with the usual assumption that spins of BHs are static from formation to merger.

Bibliography

[1] B. P. Abbott *et al.*, Physical Review Letters **116**, 061102 (2016).

[2] B. P. Abbott *et al.*, Physical Review Letters **119**, 161101 (2017).

[3] W. M. Farr *et al.*, Nature **548**, 426 (2017).

[4] C. L. Rodriguez, M. Zevin, C. Pankow, V. Kalogera, and F. A. Rasio, The Astrophysical Journal **832**, L2 (2016).

[5] B. Farr, D. E. Holz, and W. M. Farr, The Astrophysical Journal **854**, L9 (2018).

[6] J. Michell, Philosophical Transactions of the Royal Society of London Series I **74**, 35 (1784).

[7] K. Schwarzschild, Sitzungsberichte der Königlich Preussischen Akademie der Wissenschaften **18**, 424 (1916).

[8] R. P. Kerr, Physical Review Letters **11**, 237 (1963).

[9] G. E. Brown, C.-H. Lee, R. A. M. J. Wijers, and H. A. Bethe, Physics Reports **333**, 471 (2000).

[10] A. Einstein, Sitzungsberichte der Königlich Preußischen Akademie der Wissenschaften (Berlin), Seite 688-696. (1916).

[11] B. P. Abbott *et al.*, The Astrophysical Journal **848**, L12 (2017).

[12] A. Einstein, Sitzungsberichte der Königlich Preußischen Akademie der Wissenschaften (Berlin), Seite 154-167. (1918).

[13] R. A. Hulse and H. J. Taylor, in *Bulletin of the American Astronomical Society*, Vol. 6 of *Bulletin of the American Astronomical Society* 1974, p. 453.

[14] J. H. Taylor and J. M. Weisberg, Astrophysical Journal **253**, 908 (1982).

[15] K. Tsubono, in *First Edoardo Amaldi Conference on Gravitational Wave Experiments*, edited by E. Coccia, G. Pizzella, and F. Ronga 1995.

[16] K. Danzmann *et al.*, in *First Edoardo Amaldi Conference on Gravitational Wave Experiments*, edited by E. Coccia, G. Pizzella, and F. Ronga 1995.

[17] A. Abramovici *et al.*, Science **256**, 325 (1992).

[18] B. Caron *et al.*, Nuclear Instruments and Methods in Physics Research A **360**, 258 (1995).

[19] L. Blanchet, G. Faye, and B. F. Whiting, Physical Review D **90**, 044017 (2014).

[20] F. Pretorius, Physical Review Letters **95**, 121101 (2005).

[21] LIGO Scientific Collaboration *et al.*, Classical and Quantum Gravity **32**, 074001 (2015).

[22] B. Paczynski, in *Structure and Evolution of Close Binary Systems*, Vol. 73 of *IAU Symposium*, edited by P. Eggleton, S. Mitton, and J. Whelan 1976, p. 75.

[23] I. Iben, Jr. and M. Livio, Publications of the Astronomical Society of the Pacific **105**, 1373 (1993).

[24] P. Podsiadlowski, in *Evolution of Binary and Multiple Star Systems*, Vol. 229 of *Astronomical Society of the Pacific Conference Series*, edited by P. Podsiadlowski, S. Rappaport, A. R. King, F. D'Antona, and L. Burderi 2001, p. 239.

[25] R. Voss and T. M. Tauris, Monthly Notices of the Royal Astronomical Society **342**, 1169 (2003).

[26] V. Kalogera, K. Belczynski, C. Kim, R. O'Shaughnessy, and B. Willems, Physics Reports **442**, 75 (2007).

[27] R. E. Taam and P. M. Ricker, New Astronomy Reviews **54**, 65 (2010).

[28] M. Dominik *et al.*, Astrophysical Journal **759**, 52 (2012).

[29] M. Dominik *et al.*, Astrophysical Journal **779**, 72 (2013).

[30] N. Ivanova *et al.*, Astronomy & Astrophysics **21**, 59 (2013).

[31] K. A. Postnov and L. R. Yungelson, Living Reviews in Relativity **17**, 3 (2014).

[32] K. Belczynski, D. E. Holz, T. Bulik, and R. O'Shaughnessy, Nature **534**, 512 (2016).

[33] J.-P. Zahn, Astronomy & Astrophysics **220**, 112 (1989).

[34] R. G. Izzard, E. Ramirez-Ruiz, and C. A. Tout, Monthly Notices of the Royal Astronomical Society **348**, 1215 (2004).

[35] R. G. Detmers, N. Langer, P. Podsiadlowski, and R. G. Izzard, Astronomy & Astrophysics **484**, 831 (2008).

[36] S. E. de Mink *et al.*, Astronomy & Astrophysics **497**, 243 (2009).

[37] M. Cantiello, S.-C. Yoon, N. Langer, and M. Livio, in *Unsolved Problems in Stellar Physics: A Conference in Honor of Douglas Gough*, Vol. 948 of *American Institute of Physics Conference Series*, edited by R. J. Stancliffe, G. Houdek, R. G. Martin, and C. A. Tout 2007, pp. 413–418.

[38] W. Packet, Astronomy & Astrophysics **102**, 17 (1981).

[39] S. E. de Mink, N. Langer, R. G. Izzard, H. Sana, and A. de Koter, Astrophysical Journal **764**, 166 (2013).

[40] V. Kalogera, Astrophysical Journal **541**, 319 (2000).

[41] P. Marchant, N. Langer, P. Podsiadlowski, T. M. Tauris, and T. J. Moriya, Astronomy & Astrophysics **588**, A50 (2016).

[42] I. Mandel and S. E. de Mink, Monthly Notices of the Royal Astronomical Society **458**, 2634 (2016).

[43] S. E. de Mink and I. Mandel, Monthly Notices of the Royal Astronomical Society **460**, 3545 (2016).

[44] S. Sigurdsson and L. Hernquist, Nature **364**, 423 (1993).

[45] S. F. Portegies Zwart and S. L. W. McMillan, The Astrophysical Journal **528**, L17 (2000).

[46] J. M. B. Downing, M. J. Benacquista, M. Giersz, and R. Spurzem, Monthly Notices of the Royal Astronomical Society **407**, 1946 (2010).

[47] J. M. B. Downing, M. J. Benacquista, M. Giersz, and R. Spurzem, Monthly Notices of the Royal Astronomical Society **416**, 133 (2011).

[48] B. M. Ziosi, M. Mapelli, M. Branchesi, and G. Tormen, Monthly Notices of the Royal Astronomical Society **441**, 3703 (2014).

[49] C. L. Rodriguez *et al.*, Physical Review Letters **115**, 051101 (2015).

[50] C. L. Rodriguez, C.-J. Haster, S. Chatterjee, V. Kalogera, and F. A. Rasio, The Astrophysical Journal **824**, L8 (2016).

[51] WikimediaCommons, File:Field tidal.svg - Wikimedia Commons, 2014.

[52] J. N. Bahcall and R. A. Wolf, Astrophysical Journal **209**, 214 (1976).

[53] J. N. Bahcall and R. A. Wolf, Astrophysical Journal **216**, 883 (1977).

[54] A. P. Lightman and S. L. Shapiro, Astrophysical Journal **211**, 244 (1977).

[55] J. Spitzer, Lyman, Astrophysical Journal **158**, L139 (1969).

[56] G. Fragione, N. Leigh, I. Ginsburg, and B. Kocsis, ArXiv e-prints arXiv:1806.08385 (2018).

[57] B. Mockler, J. Guillochon, and E. Ramirez-Ruiz, ArXiv e-prints arXiv:1801.08221 (2018).

[58] E. Ramirez-Ruiz and S. Rosswog, Astrophysical Journal **697**, L77 (2009).

[59] J. Guillochon and E. Ramirez-Ruiz, Astrophysical Journal **809**, 166 (2015).

[60] J. K. Cannizzo, H. M. Lee, and J. Goodman, Astrophysical Journal **351**, 38 (1990).

[61] A. Ulmer, in *American Institute of Physics Conference Series* 1998, Vol. 431, pp. 141–144.

[62] S. Gezari *et al.*, Astrophysical Journal **698**, 1367 (2009).

[63] G. Lodato and E. M. Rossi, Monthly Notices of the Royal Astronomical Society **410**, 359 (2011).

[64] L. E. Strubbe and E. Quataert, Monthly Notices of the Royal Astronomical Society **415**, 168 (2011).

[65] J. Guillochon, H. Manukian, and E. Ramirez-Ruiz, Astrophysical Journal **783**, 23 (2014).

[66] H. Shiokawa, J. H. Krolik, R. M. Cheng, T. Piran, and S. C. Noble, Astrophysical Journal **804**, 85 (2015).

[67] C. Bonnerot, E. M. Rossi, G. Lodato, and D. J. Price, Monthly Notices of the Royal Astronomical Society **455**, 2253 (2016).

[68] K. Hayasaki, N. Stone, and A. Loeb, Monthly Notices of the Royal Astronomical Society **461**, 3760 (2016).

[69] J. Samsing, M. MacLeod, and E. Ramirez-Ruiz, Astrophysical Journal **784**, 71 (2014).

[70] C. L. Rodriguez, S. Chatterjee, and F. A. Rasio, Physical Review D **93**, 084029 (2016).

[71] P. P. Eggleton, Astrophysical Journal **268**, 368 (1983).

[72] J. M. Bardeen, Nature **226**, 64 (1970).

[73] V. Springel, Monthly Notices of the Royal Astronomical Society **364**, 1105 (2005).

[74] R. Pakmor, P. Edelmann, F. K. Röpke, and W. Hillebrandt, Monthly Notices of the Royal Astronomical Society **424**, 2222 (2012).

[75] A. Batta, E. Ramirez-Ruiz, and C. Fryer, Astrophysical Journal **846**, L15 (2017).

[76] J. Guillochon and E. Ramirez-Ruiz, Astrophysical Journal **767**, 25 (2013).